POLISH MARITIME RESEARCH 3 (115) 2022 Vol. 29; pp. 33-46
10.2478/pomr-2022-0023

ASSISTED PROPULSION DEVICE OF A SEMI-SUBMERSIBLE SHIP BASED ON THE MAGNUS EFFECT

Jingze Lv
Yiqun Lin
Rui Zhang
Boyang Li *
Hualin Yang
College of Electromechanical Engineering, Qingdao University of Science and Technology, China
* Corresponding author: *qdlby@126.com (Boyang Li)*

ABSTRACT

The purpose of this study is to explore the potentiality of wind propulsion on semi-submersible ships. A new type of Flettner rotor (two rotating cylinders) system installed on a semi-submersible ship is proposed. The structure and installation of two cylinders with a height of 20 m and a diameter of 14 m are introduced. The numerical simulation of the cylinder is carried out in Fluent software. The influence of apparent wind angle and spin ratio on the two cylinders are analysed, when the distance between two cylinders is 3D-13D (D is cylinder diameter). When the distance between two cylinders is 3D, the performance of the system increases with an increase in spin ratio. Moreover, the apparent wind angle also has an effect on the system performance. Specifically, the thrust contribution of the system at the apparent wind angle of 120° is the largest at the spin ratio of 3.0. The maximum thrust reaches 500 kN. When the spin ratio is 2.5 and the apparent wind angle is 120°, the maximum effective power of the system is 1734 kW. In addition, the influence of the two cylinders distance on system performance cannot be ignored. When the distance between the two cylinders is 7D and the spin ratio is 2.5, the effective power of the system reaches a maximum, which is 1932 kW.

Keywords: Flettner rotor, Semi-submersible ship, Wind energy, Ship propulsion, Numerical simulation

NOMENCLATURE

Symbol	Denomination
D	Diameter of the rotating cylinder
H	Height of rotating cylinder
S	Cross-sectional area of rotating cylinder
ρ	Fluid density
v	Kinematic viscosity is 1.45*10-5 pa/s
$Vship$	Ship speed
$Vwind$	Environmental wind speed
Va	Apparent wind speed
$Utan$	Tangential velocity of rotating cylinder
$\alpha = \frac{U_{tan}}{V_a}$	Spin ratio
X	Distance between two cylinders
$y+$	A non-dimensional wall distance
θ	Apparent wind angle

Symbol	Denomination
CL	Lift coefficient
CD	Drag coefficient
CT	Thrust coefficient
CH	Heel coefficient
FT	Thrust force
FH	Side force from heel
PT	Thrust power
CM	Moment coefficient
$Pmotor$	Power consumption
Pef	Effective power
P	Static pressure
P_{∞}	Free flow pressure
$C_p=\frac{P-P_{\infty}}{0.5*\rho*{V_a}^2}$	Pressure coefficient

INTRODUCTION

With the exhaustion of oil resources and the deterioration of the environment, more and more countries are paying attention to the development of renewable energy. At the same time, stricter requirements for ship emissions have been put forward by the International Maritime Organization (IMO) [1-3]. Therefore, it is urgent to develop energy conservation & emission reduction technologies by using renewable energy or clean energy. Renewable energy is widely used in ships. Nowadays, the renewable energy used on ships mainly includes solar energy and wind energy [4,5]. Of these, wind energy is characterised by wide distribution and abundant reserves [6]. Besides this, flat sea levels have less resistance to the wind and so wind energy at sea is more abundant. The utilisation of wind energy in ships has unique advantages [7].

In order to realise the utilisation of wind energy in ships, scholars have studied a variety of devices to capture wind energy. The mature wind energy utilisation devices mainly include: traditional sails, airfoil sails, kite sails and Flettner rotors [8-10]. The Flettner rotor is an effective device for capturing wind energy on ships [11,12]. The device was first installed on ships one hundred years ago. The Flettner rotor relies on a drive system to achieve rotation. When the wind is coming from one side, the rotation of the rotor causes the wind speed on both sides of the rotor to be changed. Based on Bernoulli's principle, there will be a pressure difference between the two sides of the cylinder, so the lift generated by the cylinder can provide assisted thrust for the ship. The lift is also called a Magnus force and this phenomenon is known as the Magnus effect.

Flettner rotors have been installed on actual ships. The Flettner rotor was first installed and tested on the German ship 'Buckau' in 1924. Recently, an ore carrier also installed Flettner rotors to reduce fuel consumption. Related simulations and experiments on Flettner rotors have been studied by scholars [13-15]. Lu et al. [11] proposed three wind energy utilisation technologies (Flettner rotor, wingsail and DynaRig concept) and selected an Aframax Oil Tanker as a model to compare three kinds of technologies. They found that the three technologies contributed to saving 5.6-8.9% of fuel, the Flettner rotor having the best fuel-saving function. Tillig et al. [12] analysed a total of 11 different arrangements of Flettner rotors in the tanker and RoRo ship. The study showed that tankers saved 30% fuel and the RoRo ship saved 14% fuel. Thus, the Flettner rotor has become an effective propulsion device in ship navigation. In order to identify the most influencing parameters on Flettner rotor performance, De Marco et al. [16] analysed the influence of spin ratio, aspect ratio and end plate on the Flettner rotor. It was found that spin ratio is the most important factor affecting rotor performance. Li et al. [17] proposed that a deformed sail and a 300,000-ton oil tanker was used as the base ship. They found that the 16-sided sail had better performance and the peak value of lift for the sail was 590 kN. Bordogna et al. [18] studied the influence of Reynolds number on the performance of the cylinders through large wind tunnel tests. For the performance of the cylinders, it was a key point for the spin ratio of 2.5. Bordogna et al. [19] studied the aerodynamic interaction effect of two Flettner rotors through wind tunnel test. The results showed that the distance and spin ratio are the most important factors affecting the aerodynamic performance of two cylinders. Li et al. [20] proposed a new Flettner rotor and, on the basis of not occupying the deck area, the device obtained a better performance than the Flettner rotor. They found that the maximum thrust can reach 750 kN for a 100,000-ton ship.

Flettner rotors usually work in side-winds and the performance of the rotor primarily depends on the environment, wind and ship speed. In practical installations, ships are usually equipped with multiple Flettner rotors to greater use wind energy. The diameter of the Flettner rotor is 1.5-5.0 m and its height is 15-40 m [21,22]. In addition, according to the condition of the Magnus effect, the wind-receiving area of the Flettner rotor affects its performance. The larger the wind-receiving area of the Flettner rotor, the greater the thrust [23,24]. However, the Flettner rotor has a larger wind-receiving area, which can occupy the deck area. This is a disadvantage for ships with high deck utilisation [25]. So, it will be of great significance to design a new Flettner rotor which can assist the navigation of ships but also save on deck area.

Currently, Flettner rotors are mostly installed in merchant ships, but a few have been installed in special ships. The semi-submersible ship is a kind of special ship which transports cargo, with a super large size that cannot be divided. Fig. 1 shows the semi-submersible ship 'Xin Guang Hua' of COSCO SHIPPING. When a semi-submersible ship is transporting cargo from one port to another, it is usually empty on the return journey: Port A to port B is free of cargo, or port B to port A is free of cargo. Half of the ship's working time is ballast voyage (ballast voyage means that there is no cargo on deck). An empty deck makes the Flettner rotors on a semi-submersible have a better chance of harnessing wind energy. Secondly, due to the low centre of gravity of the semi-submersible ship, the installation of Flettner rotors has little effect on the stability of the ship during the voyage. Therefore, the Flettner rotors installed on a semi-submersible ship have great advantages. However, if the Flettner rotors are installed directly on the deck, the deck area will be occupied, thus affecting the cargo transport of the semi-submersible ship. In addition, the semi-submersible ship has two pontoons on the deck to adjust the ship's draft. If the pontoons are combined with the Flettner rotors, the Flettner rotors can use the wind energy to provide part of the ship's thrust without occupying the deck area. Based on the above discussion, in this study, the installation and method of use of a new type of Flettner rotor is proposed. The new Flettner rotor system is an assisted propulsion device. The two pontoons of a semi-submersible ship and two rotating cylinders are cleverly combined. Two huge rotating cylinders were created without affecting the function of the pontoons. The advantage of these rotating cylinders is that they do not occupy the deck area and can increase the wind-receiving area of the rotating cylinders, so that the rotor can better apply wind energy. In general, Flettner rotors have the potential to save 3% to 25% of engine fuel consumption. This is of economic value to semi-submersible ships.

Fig. 1. The semi-submersible ship 'Xin Guang Hua'

THE STRUCTURE AND INSTALLATION OF THE NEW TYPE OF FLETTNER ROTOR SYSTEM

In order to analyse the contribution of the new type of Flettner rotor system, the semi-submersible ship 'Xin Guang Hua' of COSCO SHIPPING was selected as an example. This is one of the largest semi-submersible ships in the world and is typical for its kind. The structure of the new type of Flettner rotor system is shown in Fig. 2(a). Two huge rotating cylinders are set on the outside of two pontoons, respectively. Fig. 2(b) shows the composition of one of the rotating cylinders. It is a circular hollow cylinder with an end plate, enveloped on the outside of the pontoon. A motor drives the rotating cylinder to achieve its function without affecting the function of the pontoon. Moreover, in order to avoid interfering with the ship's crew passing the pontoon, the bottom of the rotating cylinder is placed 2 m away from the deck; the top of the rotating cylinder is placed on the upper of the pontoons. When the ship is sailing, the wind coming from one side of the rotating cylinder will generate the Magnus effect. Fig. 2(c) shows the installation position of the new Flettner rotor system on the semi-submersible ship. Fig. 2(c_1) shows two rotating cylinders installed side by side, in which the distance of the two rotating cylinders X=3D. This is a typical case, which will be described in detail in this study. In addition to this, the pontoons on the deck can move along the sliding rail. Therefore, the boosting effect of two rotating cylinders at different positions was studied when the ship is sailing with no load or transporting cargo of small size. Figs. 2(c_2)-(c_4) show two rotating cylinders installed in different positions; to be specific, the distance of the two rotating cylinders X>3D.

The new type of Flettner rotor system is superior in a number of ways. On the one hand, the rotating cylinders are installed on the pontoons, which can realise the utilisation of wind energy without occupying the area of the deck. On the other hand, due to the large size of the pontoons, the rotating cylinders installed on the outside of the pontoons have a larger wind-receiving area than the conventional Flettner rotor. The larger wind-receiving area increases the lift generated by the rotating cylinders.

In this analysis, a 100,000-ton semi-submersible ship, Xin Guang Hua, was selected as an example for simulation. Table 1 shows some of its parameters. The height of the pontoons on the semi-submersible ship was 20 m. In order not to affect the functions of the semi-submersible ship's transportation cargo, the diameter of the rotating cylinders should be as close to the pontoons as possible. The diameters of the rotating cylinders were 14 m. In addition, the height of the rotating cylinders was 20 m and the diameters of the end plate were 28 m.

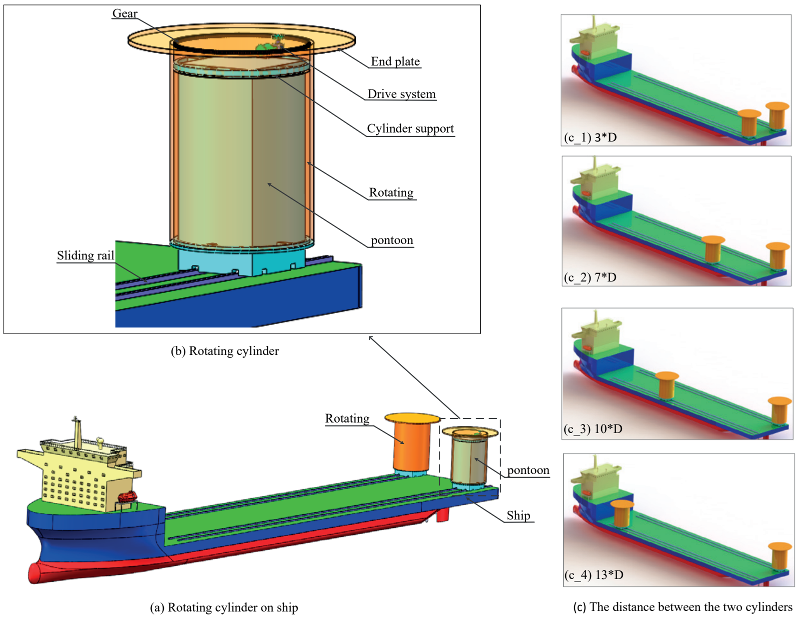

(b) Rotating cylinder

(a) Rotating cylinder on ship

(c) The distance between the two cylinders

Fig. 2. The new Flettner rotor system and its installation position on the ship

Tab. 1. Parameters of 'Xin Guang Hua'

Parameter	Value (m)	Parameter	Value
Length overall	255.0	Deadweight (tonne)	98500
Breadth moulded	68.0	Main engine power (kw)	21300
Depth	14.5	Maximum speed (knots)	14.5
Draft	10.5	Effective deck area (m2)	14280

GEOMETRICAL CONFIGURATION

PHYSICAL MODELS

When the ship is affected by environmental wind (Vwind), the Magnus force generated by the rotating cylinder will provide part of the thrust for the ship. As shown in Fig. 3, when wind is coming from the port side of the ship, the two rotating cylinders rotate clockwise and generate a forward thrust. Similarly, when wind is coming from the starboard side of the ship, the two rotating cylinders rotate counter-clockwise and also produce a forward thrust, according to the Magnus effect. Therefore, in order to ensure that the thrust from the rotating cylinder reaches its peak value along the traveling direction of the ship, a wind direction sensor can be installed to obtain the wind direction at this time, so as to control the rotation of the rotating cylinders. In addition to this, the apparent wind acting on the rotating cylinders is an important factor for verifying the performance of the new type of Flettner rotor system. As shown in Fig. 3(a), the apparent wind acting on the rotating cylinders is the vector sum of the ship speed and the environmental wind speed. The apparent wind acting on the rotating cylinders can be obtained by Eq. (1). In the following simulation, the apparent winds in different directions were considered; the environmental wind speed was 10 m/s and the ship speed was 5 m/s.

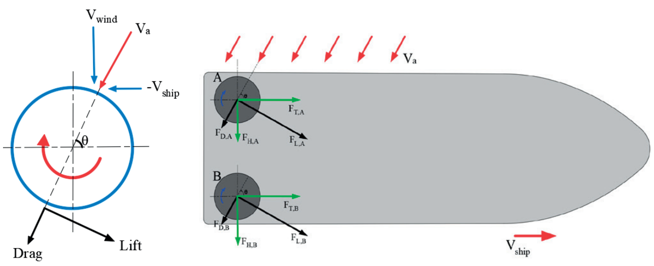

(a) (b)

Fig. 3. The apparent wind (a) and force generated by the cylinders (b)

As shown in Fig. 3, in the course of the ship's voyage, the thrust (*CT*) and heel (*CH*) coefficients are determined by the lift (*CL*) and drag coefficients (*CD*) of the rotating cylinder and the apparent wind angle between the heading and the apparent wind speed. The equations of thrust coefficient and heel coefficient are given as follows [14]:

$$V_a = V_{wind} - V_{ship} \tag{1}$$

$$C_T = C_L * \sin(\theta) - C_D * \cos(\theta) \tag{2}$$

$$C_H = C_L * \cos(\theta) + C_D * \sin(\theta) \tag{3}$$

The thrust (*FT*) and side force from the heel (*FH*) are calculated according to thrust coefficient (*CT*), heel coefficient (*CH*), apparent wind speed (*Va*) air density (ρ) and Cross-sectional area of the rotating cylinder (*S*), according to the Eqs. (4) and (5). Fig. 3(b) shows the diagram of ship forces.

$$F_T = 0.5 * \rho * S * {V_a}^2 * C_T \tag{4}$$

$$F_H = 0.5 * \rho * S * {V_a}^2 * C_H \tag{5}$$

The thrust generated by the rotating cylinders is the vector sum of lift and drag. According to the thrust (*FT*), ship speed (*Vship*), spin ratio (α), and torque coefficient (*CM*), the thrust power generated by the rotating cylinders and the power consumed by the motor are calculated in Eqs. (6) and (7) [26].

$$P_T = T * V_{ship} \tag{6}$$

$$P_{motor} = 0.5 * \rho * S * {V_a}^3 * C_M * \alpha \tag{7}$$

The effective power generated by the rotating cylinder is determined by the power consumed by the motor and the lift / drag acting on the rotating cylinder. The effective power *Pef* is given by Eq. (8).

$$P_{ef} = P_T - P_{motor} \tag{8}$$

COMPUTATIONAL DOMAIN AND GRID GENERATION

In order to obtain lift coefficients, drag coefficients and propulsive power of the two rotating cylinders, the CFD (Computational Fluid Dynamics) software 'Fluent' was used to calculate the RANS equation, in conjunction with the Realisable k-ε turbulence model [27-29]. From Eqs. (9) and (10), the RANS equation included the continuity equation and momentum equation are given as:

$$\nabla \cdot U = 0 \tag{9}$$

$$\rho \bar{u}_j \frac{\partial \bar{u}_i}{\partial x_j} = \rho \bar{f}_i + \frac{\partial}{\partial x_i}\left[-\bar{p}\delta_{ij} + \mu\left(\frac{\partial \bar{u}_i}{\partial x_j} + \frac{\partial \bar{u}_i}{\partial x_i}\right) - \rho\overline{u_I{}' \; u_J{}'}\right] \tag{10}$$

where ρ is the density of the fluid; μ is fluid viscosity; δ_{ij} is Kronecker delta; *U* is the relative velocity; $\bar{f}_i$ is the mass force term; $\bar{p}$ is static pressure; and $-\rho\overline{u_I u_j}$ is the apparent stress resulting from the fluctuating velocity field, generally referred to as the Reynolds stress.

The computational domain and boundary condition for the two rotating cylinders are given in Fig. 4. The whole computational domain shape is a similar cylinder, which has a diameter of 15 X. X is the distance between the centres of the two rotating cylinders. The thickness of the computational domain is four times that of the rotating cylinders. The two rotating cylinders are installed symmetrically in the central region of the computational domain. The two rotating cylinders are surrounded by two 2*D rotating domains (D is the diameter of the rotating cylinder), which are used to represent the wind field generated by the rotating cylinders [30]. The inlet boundary is set on the left side of the calculational domain, which adopts the Velocity-inlet; the outlet boundary is set on the right side of the calculational domain, which adopts the Pressure-outlet and the value is 1.103*105 pa. The other four faces of the computational domain are defined as walls.

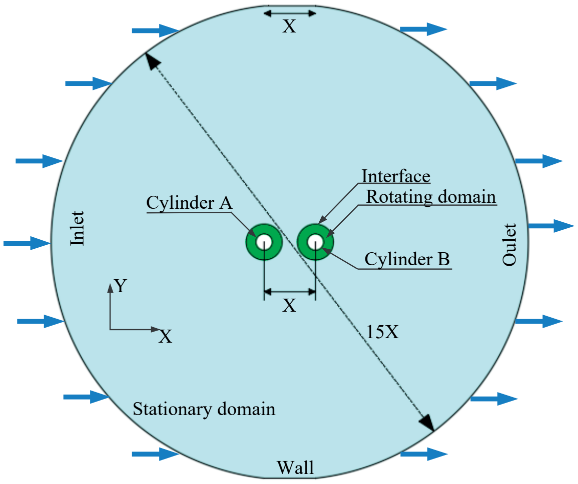

Fig. 4. Computational domain and boundary condition

The rotating cylinder with an endplate is shown in Fig.5 (a). The rotating cylinder with an endplate is shown. For the whole computational domain, the coupling unstructured and structured grids are adopted; to be specific, tetrahedral grids are used for the rotating domains and hexa-grids are used for the whole domain. The 2*D range near the two cylinders forms the rotating domain, as shown in Fig. 5(b). The two rotating cylinders rotate clockwise. The surfaces of the two rotating cylinders are set as non-slip walls which have a certain roughness. The sliding grid is used in this rotating domain. As shown in Fig. 5(c), in order to simulate the rotation of the cylinder more accurately, a prismatic mesh layer is used on the wall of the rotating cylinder. There are five prism layers, with a layer growth rate of 1.2. Besides, the non-dimensional wall distance ($y+$) is approximately equal to 1, which meets the requirements of the turbulence model; the blockage ratio of this model is about 1.6%. The left rotating cylinder is defined as cylinder *A* and the right rotating cylinder as cylinder *B*. In addition, the positive direction of the y-axis is the sailing direction of the ship and the port-wind is the focus of attention.

GRID INDEPENDENCE ANALYSIS

The grid independence was tested by using four grid densities of approximately 1,500,000, 200,000, 2,500,000, and 4,000,000 cells. The pressure coefficient *Cp* of cylinder A was used to compare different grids. The other verification simulations assumed that: the apparent wind angle is 90°, the environment wind is 10 m/s, the ship speed is 5 m/s, and the spin ratio α is 2.0. The instantaneous *Cp* is presented in Fig 6. The average *Cp* is listed in Table 2. When the grid reaches 2.5 million cells, further increasing the grid density has little effect on the results. When compared with the case of 4 million cells, the error of the *Cp* is less than 0.44%. Therefore, considering accuracy and efficiency, 2.5 million grids were selected for subsequent simulation.

Tab. 2. The average Cp of different grids

Grid number	**Average *Cp* (30-60s)**	**Error of average-*Cp***
1,500,000	-2.00971	3.52%
2,000,000	-2.02827	2.63%
2,500,000	-2.07382	0.44%
4,000,000	-2.08309	0.00%

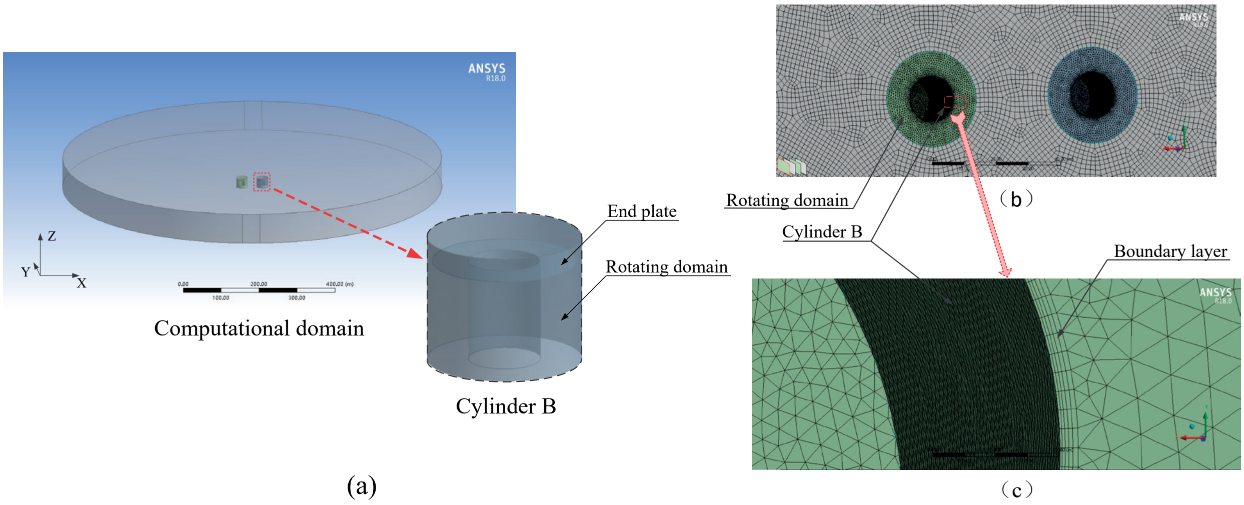

(a)

（b）

（c）

Fig. 5. Grid configuration for the cylinder

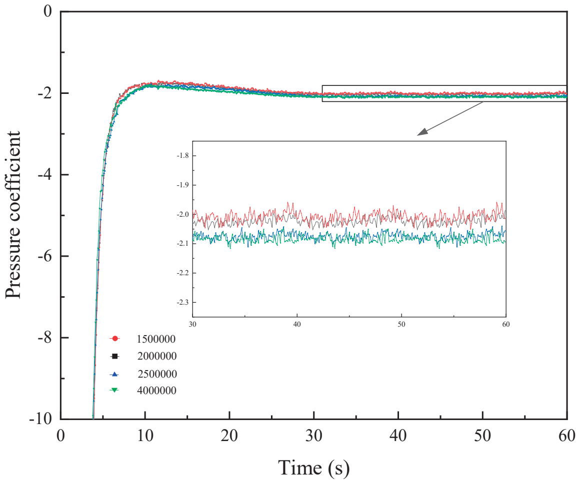

Fig. 6. Data curves of instantaneous Cp

COMPARISON OF EXPERIMENTAL DATA AND SIMULATION DATA

Comparison between simulation data and experimental data is shown in Fig. 7. Experimental data were obtained from Badalamenti et al. [31]. According to their research, the conditions selected for simulation were: the cylinder diameter (88.9 mm), cylinder length (450 mm), wind speed (7 m/s), diameter of end plate (177.8 mm), and selected spin ratios (0.0, 0.5, 1.0, 2.0 and 3.0, respectively). The lift coefficient and drag coefficient of the cylinder were compared. The errors between the simulation and experimental data are presented in Table 3. It can be seen that the numerical results were found to be a good match with the experimental data. The simulation settings in this study are the same as those used for simulation validation. Therefore, the numerical method is acceptable.

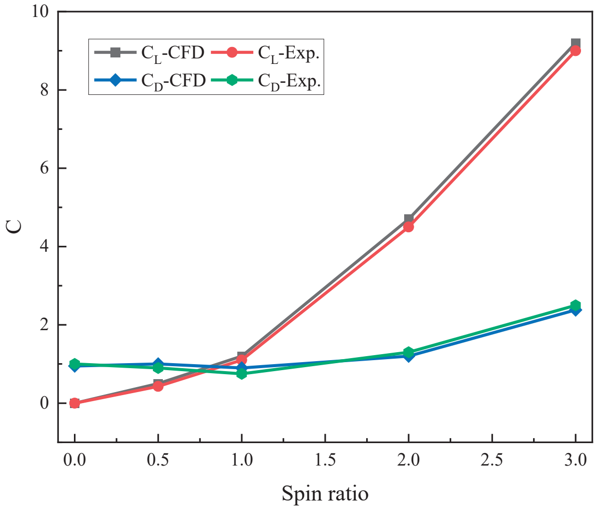

Fig. 7. Comparison of CL and CD for the numerical data and the experimental data

Tab. 3. CL and CD percentage error between numerical and experimental data

Spin ratio	0.0	0.5	1.0	2.0	3.0
CL	/	16.2%	9.0%	4.4%	3.1%
CD	5%	11.1%	20.0%	7.6%	4.8%

The aspect ratio of the rotor in the above experiment was 5, while the aspect ratio of the new rotor proposed in this study was 1.4. Then, in order to better test the accuracy of the simulation settings, rotors with similar aspect ratios were selected for comparison. The simulation results were compared with the results reported by De Marco et al. [32]. The conditions selected for simulation were: cylinder diameter (4 m), end plate diameter (8 m), cylinder length (14 m), and the angular speed of the rotor (10 rad/s). The results of the data comparison are shown in Fig. 8. The numerical data are close to the reference data and, therefore, the simulation settings are acceptable.

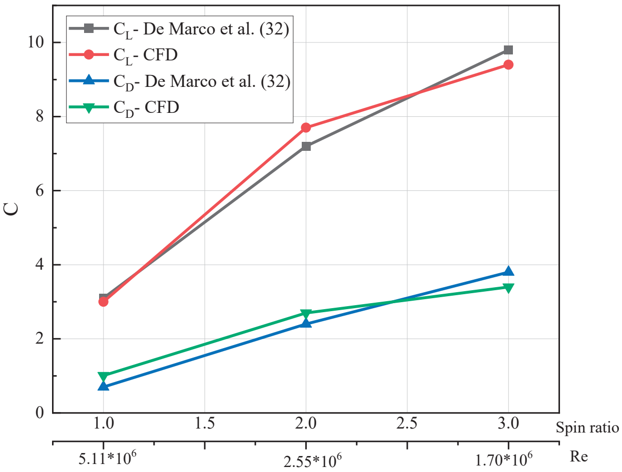

Fig. 8 Comparison of CL and CD for the numerical data and the reference data

ANALYSIS OF RESULTS

When the semi-submersible ship is sailing at sea, the two rotating cylinders are installed side by side at the stern. Its location is shown in Fig. 2(c_1). This is a typical condition when the ship is sailing. In order to verify the boosting effect of the rotating cylinders, the lift coefficients, drag coefficients and other parameters of the two rotating cylinders under different spin ratios were studied, when the apparent wind angle was 30°, 60°, 90°, 120° and 150°. The thrust contribution of the rotating cylinders was also studied. The section titled «Discussion of two rotating cylinders in different positions» below, briefly discusses and verifies the effect of distance on the performance of two rotating cylinders. The different positions of the two rotating cylinders on the deck are shown in Figs. 2(c_2)-(c_4).

DISCUSSION OF TWO ROTATING CYLINDERS SIDE BY SIDE

According to the relevant studies [33,34], the change of spin ratio and apparent wind angle will affect the boosting effect of the rotating cylinders. In order to explore the performance of rotating cylinders under different apparent wind angles and different spin ratios, the influence of the spin ratio on rotating cylinders under different apparent wind angles is discussed in this section.

The lift coefficient and drag coefficient

The lift coefficients (*CL*) and drag coefficients (*CD*) of two rotating cylinders at different spin ratios are given in Fig. 9. The lift coefficients of cylinder *A* and cylinder *B* are shown in Fig. 9(a) and (b), respectively. It can be seen that the spin ratio has an important effect on the performance of two rotating cylinders. The lift coefficients of the two rotating cylinders increase with the increase of the spin ratio. Secondly, by comparing the lift coefficients of the two rotating cylinders, it can be seen that the lift coefficient of cylinder *B* is less than that of cylinder *A*, under the same conditions. This may be because cylinder *B* is partially immersed in the wake of cylinder *A*, so the lift coefficient of cylinder *B* is affected by cylinder *A*. In addition, the apparent wind angle has an effect on the two rotating cylinders. When the spin ratio of two cylinders is the same, the lift coefficient is the smallest when the apparent wind angle is 90°. The maximum lift coefficients of the two rotating cylinders are obtained at θ=150° and α=3.0. The maximum value of cylinder *A* is 11.98; the maximum value of cylinder *B* is 10.68.

Fig. 9(c) and (d) represent the drag coefficients of cylinder *A* and cylinder *B*, respectively. In Fig. 9(c), the effect of cylinder *B* leads to different variation trends of the drag coefficient of cylinder *A* with a change of spin ratio. When the apparent wind angle is 30° and 150°, as the spin ratio increases, the drag coefficient of cylinder *A* first increases and then decreases. The maximum value of drag coefficient is 2.26, at a spin ratio of 2.5. In addition, the drag coefficient of cylinder *A*, under the apparent wind angle of 90°, is the smallest, compared with other angles. In Fig. 9(d), the drag coefficient of cylinder *B* increases with the increase in spin ratio. When the apparent wind angle is 90°, the drag coefficient of cylinder *B* is much larger than that of other angles.

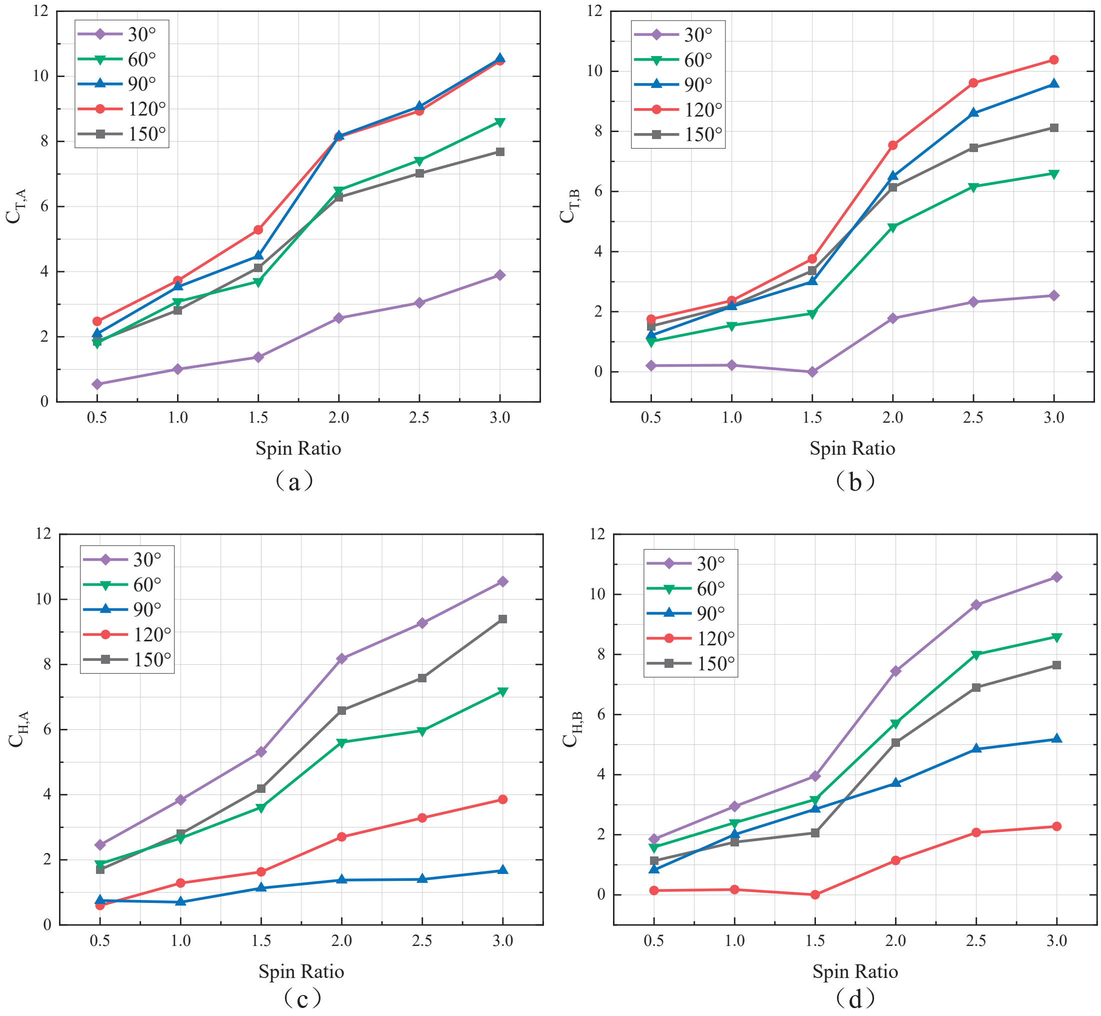

(a) (b)

(c) (d)

Fig. 9. Lift and drag coefficients for cylinder A (left) and cylinder B (right)

The thrust coefficient and heel coefficient

In order to express the thrust contribution of the rotating cylinder, intuitively, Fig. 10 shows the thrust coefficients and heel coefficients of cylinder *A* and cylinder *B*. According to Eqs. (2) and (3), the thrust and heel coefficients depend on the lift coefficient, the drag coefficient and the apparent wind angle. Fig. 10(a) and (b) show the thrust coefficients of cylinder *A* and cylinder *B*, respectively. It can be seen that the thrust coefficients of two rotating cylinders increase with the increase of the spin ratio. The maximum thrust coefficient is obtained at a spin ratio of 3.0. The maximum thrust coefficient of cylinder *A* is 10.54 when the spin ratio is 3.0 and the apparent wind angle is 90°; the maximum thrust coefficient of cylinder *B* is 10.38 when the spin ratio is 3.0 and the wind angle is 120°. Fig 10(c) and (d) show the heel coefficients of cylinder *A* and cylinder *B*, respectively. It can be seen that the heel coefficients of two rotating cylinders increase with the increase of the spin ratio. In addition, it can be seen that the heel coefficient of cylinder *A* at the apparent wind angle θ=90° is the smallest, compared with that of other angles; the heel coefficient of cylinder *B* at the apparent wind angle θ=120° is smaller than that of other angles.

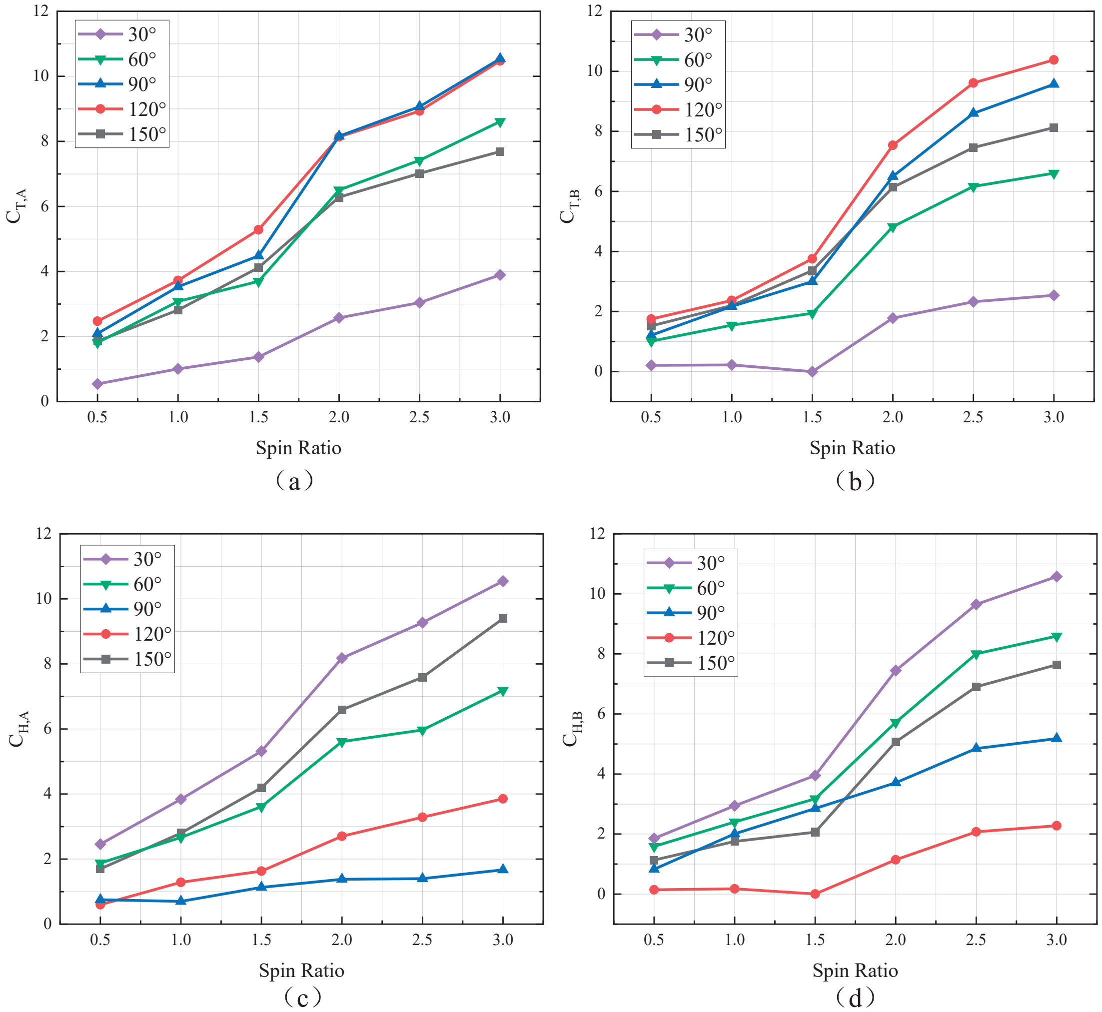

（a）（b）（c）（d）

Fig. 10. Thrust and heel coefficients for cylinder A (left) and cylinder B (right)

The pressure distributions around the cylinders

For the purpose of analysing the pressure distributions around the two rotating cylinders for different spin ratios, the pressure contours with spin ratios of 0.5-3.0, at an apparent wind angle of 90°, are given, respectively. Fig. 11 shows the pressure area around two rotating cylinders in the mid-plane under different spin ratios. It was found that two areas of low-pressure appear on the top of the two rotating cylinders. The pressure differences in the rotating cylinders will produce positive thrust to propel the ship. In addition, the pressure differences around the two rotating cylinders along the y-axis direction become larger with the increase in spin ratio. From the pressure graphs with spin ratios of 2.0, 2.5 and 3.0, the results show that the right side of cylinder *B* appears as a low-pressure area, due to the influence of cylinder *A*, and the low-pressure area becomes more obvious with the increasing spin ratio.

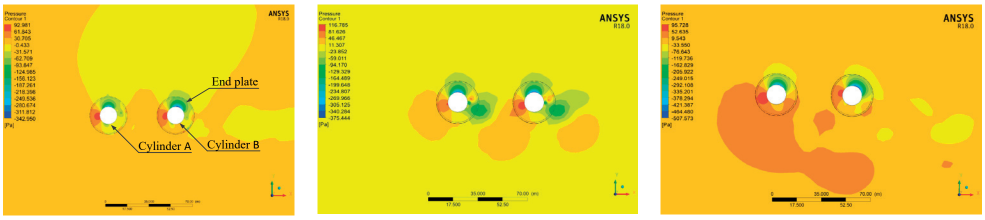

(a) Spin Ratio=0.5 (b) Spin Ratio=1.0 (c) Spin Ratio=1.5

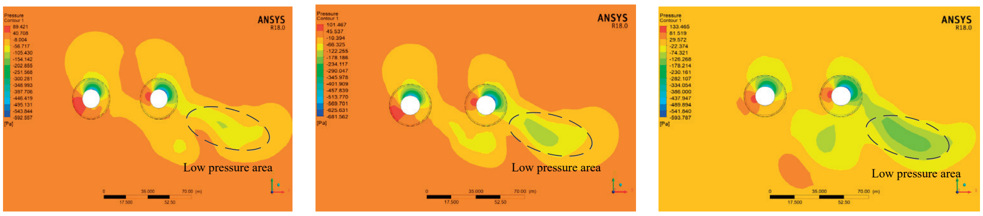

(d) Spin Ratio=2.0 (e) Spin Ratio=2.5 (f) Spin Ratio=3.0

Fig. 11. Pressure distributions of the Flettner rotor system for different spin ratios

Thrust contribution of two cylinders

The total thrust provided by the two rotating cylinders at different apparent wind angles is shown in Fig. 12. The thrust contribution is the largest at an apparent wind angle of 120° and the smallest at an apparent wind angle of 30°, in the same spin ratio. In addition, the thrust of the rotating cylinder increases with the increase in spin ratio. The maximum thrust is obtained when the spin ratio is 3.0; to be more specific, maximum thrusts of 158 kN, 375 kN, 496 kN, 515 kN and 390 kN at apparent wind angles of 30°, 60°, 90°, 120° and 150°, respectively. The thrust of the rotating cylinder reaches its maximum at the apparent wind angle of 120°, because the drag generated by the rotating cylinder at this time will also provide part of the thrust for the ship. Therefore, when the apparent wind angle $\theta > 90°$, a high drag is not a disadvantage.

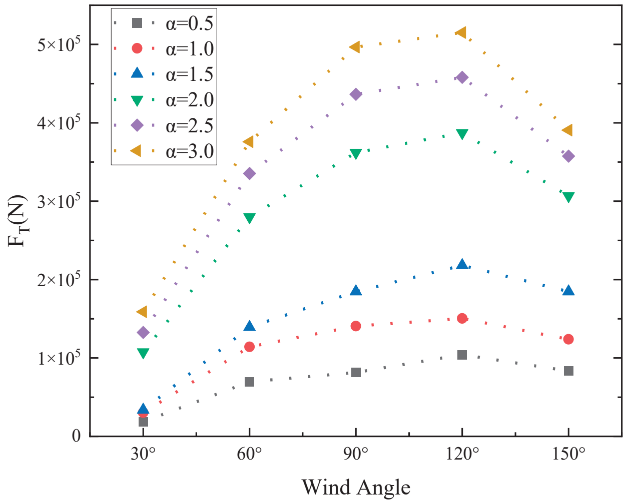

Fig. 12. The thrust contribution of the Flettner rotor system

Energy contribution of two cylinders

In order to evaluate the performance of the rotating cylinders, it is important to consider the thrust power (*PT*) and effective power (*Pef*) of the rotating cylinders. Fig. 13 shows the total thrust power and total effective power of the two rotating cylinders at different spin ratios. The thrust power and effective power are calculated by Eqs. (6)-(8). In Fig. 13, at different apparent wind angles, the thrust power rises with the increase of the spin ratio. The maximum thrust power is obtained at the spin ratio $\alpha=3.0$; to be more specific, maximum thrust power of 794 kW, 1879 kW, 2483 kW, 2575 kW and 1952 kW at apparent wind angles of 30°, 60°, 90°, 120° and 150°, respectively.

The effective power is determined by the motor consumption and the thrust power of the rotating cylinders. It provides more valuable information than thrust power. Fig. 13(a) shows the total effective power of the rotating cylinders under different spin ratios when the apparent wind angle is 30°. It can be seen that the maximum effective power reaches 241 kW at a spin ratio of 2.0. However, when the spin ratio is 3.0, the effective power is negative (which means that the thrust power is less than the power consumed by the motor), which is not good for the ship navigation. As shown in Figs. 13(b)-(e), the effective power first increases and then falls with the increase in spin ratio. In Fig. 13(b), when the spin ratio is 2.5 and the apparent wind angle is 60°, the maximum effective power is 1121 kW. The maximum effective power is 1626 kW at an apparent wind angle of 90° and under a spin ratio of 2.5. Similarly, when the apparent wind angle is 150°, the maximum effective power of the spin ratio $\alpha=2.0$ is 1237 kW. However, in Fig. 13(e), the maximum effective power corresponding to an apparent wind angle of 150° occurs at the spin ratio of 2.0, which is 1237 kW. Table 4 shows that the effective power of the two rotating cylinders can reach 65% when the apparent wind angle is 60°-150°. This proves that the thrust contribution of the rotating cylinders is far larger than the energy consumed by the motor.

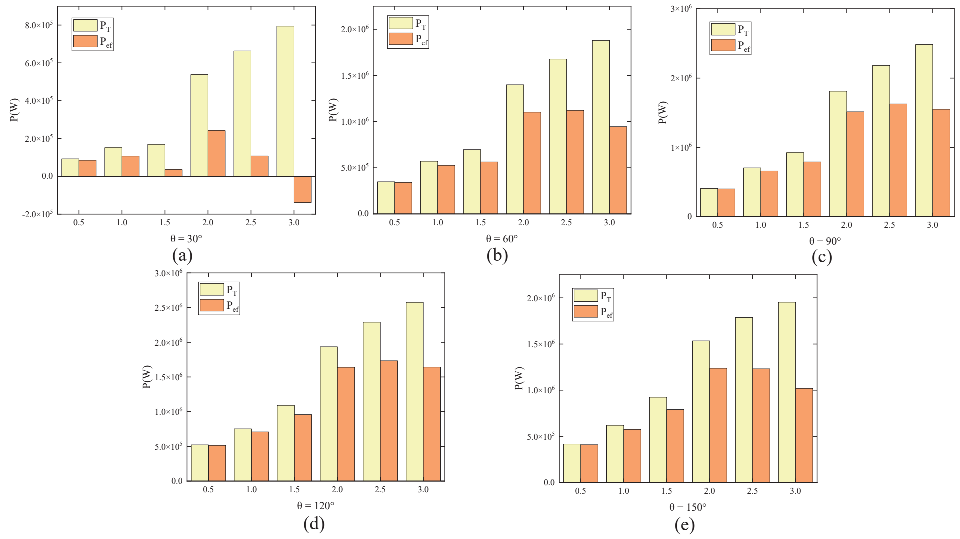

Fig. 13. The total thrust power (PT) and total effective power (Pef) of the Flettner rotor system

Tab. 4. Comparison of effective power

Apparent wind angle	Maximum effective power(W)	Spin ratio	Thrust power(W)	Effective power/ Thrust power
30°	241703	2.0	538055	44%
60°	1121633	2.5	1677293	66%
90°	1626231	2.5	2181891	74%
120°	1734140	2.5	2289800	75%
150°	1237770	2.0	1534122	80%

DISCUSSION OF TWO ROTATING CYLINDERS IN DIFFERENT POSITIONS

Since the pontoons on the deck can move along the sliding rail, the position of the two rotating cylinders can be moved according to the direction of the wind, when the semi-submersible ship is sailing with no load or transporting small cargo. The position of the two rotating cylinders is shown in Figs. 2(c_2)-(c_4). In order to study the lift coefficients, drag coefficients and power values of the rotating cylinders at different positions, the simulation condition is that the ship speed is 5 m/s and the environment wind speed is 10 m/s. The situation of apparent wind angle of 90° was selected, which is the most typical condition in semi-submersible ship navigation.

The lift coefficient and drag coefficient

Fig. 14 shows the point line graph of lift coefficients (*CL*), drag coefficients (*CD*) and lift-to-drag ratio (*CL*/*CD*) of two rotating cylinders at different positions. The spin ratio is still an important factor. The lift and drag coefficients of the two rotating cylinders increase with the increase of the spin ratio. In addition, when the spin ratio is 2.0-3.0, the lift coefficient of the cylinder *A* at a distance 7D, is larger than those at other positions. However, the lift coefficient of cylinder *B* is less than those at other positions. Figs. 14 (c) and (f) show the

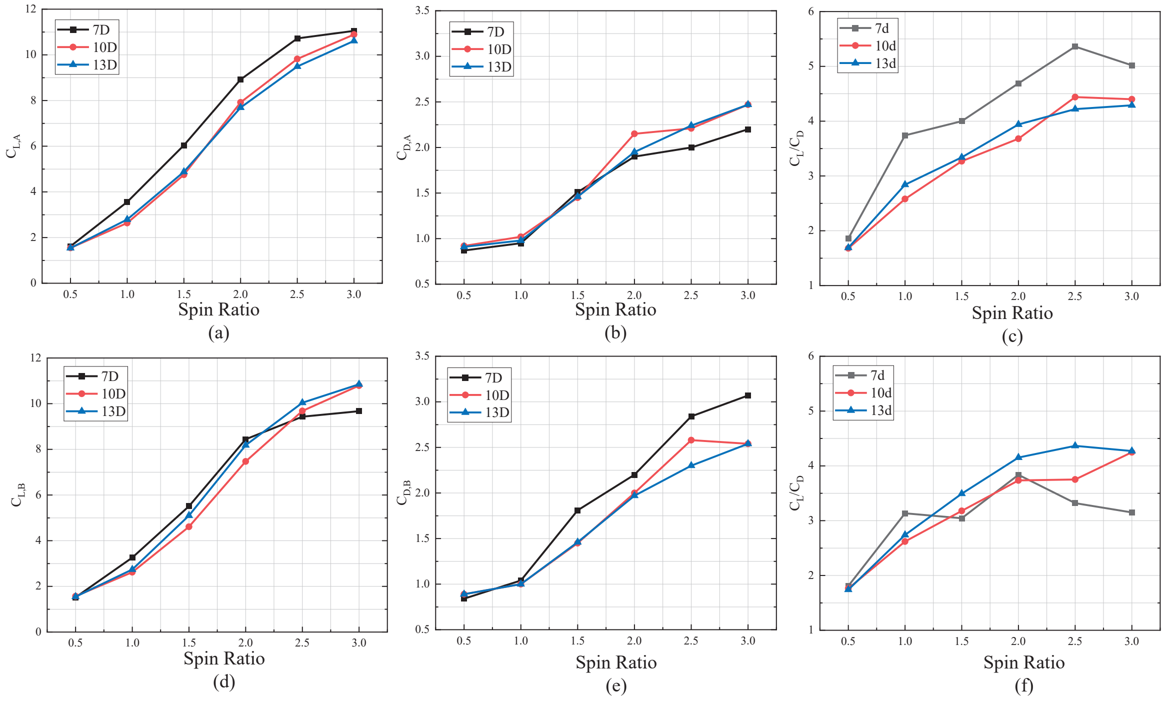

Fig. 14. Lift coefficient (a), drag coefficient (b) and lift-to-drag ratio (c) of cylinder A and lift coefficient (d), drag coefficient (e) and lift-to-drag ratio (f) of cylinder B at different positions

lift-to-drag ratios of rotating cylinders *A* and *B*, respectively. When the distance between the two rotating cylinders is 7D, there is interaction between the two rotating cylinders. The lift-to-drag ratio of cylinder *B* is less than that of cylinder *A*. When the distance between the two rotating cylinders is 10D and 13D, there is little difference in the lift-to-drag ratio of the two rotating cylinders, indicating that the influence between the two rotating cylinders is small at this distance.

Fig. 15 shows the pressure distributions at three positions with a spin ratio of 2.0. From the figure, it can be clearly seen that when the distance between the two rotating cylinders is 7D, there are two obvious low-pressure areas to the right of the two rotating cylinders. The pressure differences around the two rotating cylinders are 657 Pa along the y-axis direction. In addition to this, the pressure differences around the two rotating cylinders along the y-axis become smaller with the increase of distance. By comparing the pressure distributions, it can be found that distance is one of the important factors affecting the Magnus effect of rotating cylinders.

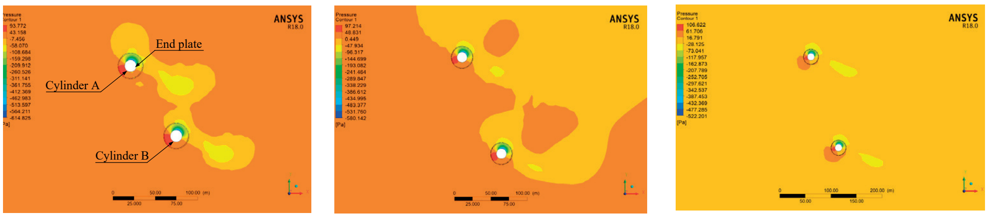

(a) Distance=7D (b) Distance=10D (c) Distance=13D

Fig. 15. Pressure distributions at different positions

Energy contribution

Fig. 16 shows the total thrust, the total thrust power and total effective power of the two rotating cylinders at different distances. The bar graph shows the total thrust power and total effective power of the rotating cylinders; the total thrust of two rotating cylinders is shown by the point line graph. It can be seen from the figure that the thrust of the two rotating cylinders increases with the increase in spin ratio. The thrust of two rotating cylinders is greatest when the distance between two cylinders is 7D and the spin ratio is 3.0. the maximum thrust is 511 kN. Similarly, when the distance is 10D and 13D, the maximum thrust reaches 535 kN and 529 kN, respectively. According to Eq. (6), it can be obtained that the maximum thrust power is 2558 kW, 2677 kW and 2649 kW at distances of 7D, 10D and 13D, respectively.

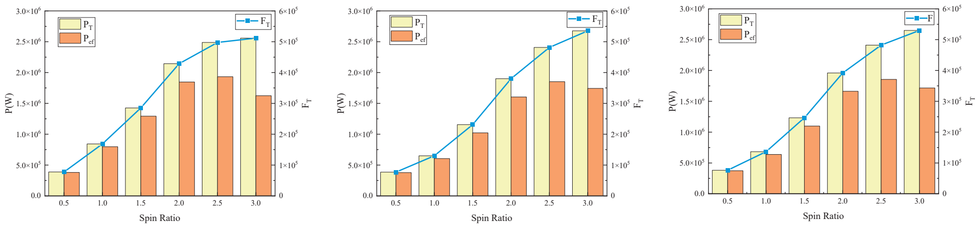

(a) X=7D (b) X=10D (c) X=13D

Fig. 16. The total thrust (FT), total thrust power (PT) and total effective power (Pef) of two rotating cylinders for different distances

By comparing the total effective power of two rotating cylinders at different positions, as the spin ratio increases, it can be found that the total effective power of the rotating cylinders first increases and then decreases. The effective power reaches the maximum at the spin ratio α=2.5. When the distance is 7D, the maximum effective power is 1932 kW. When the distance is 10D, the maximum effective power is 1852 kW. Similarly, when the distance is 13D, the maximum effective power is 1855 kW.

CONCLUSIONS

In this study, the installation and use of a new type of Flettner rotor system is proposed; where the rotating cylinders envelope is on the outside of the pontoons. When side-winds occur, the Magnus force generated by the rotating cylinders will provide power for the navigation of the ship (based on the Magnus effect). A semi-submersible ship model with two rotating cylinders is established. Under different conditions, the two rotating cylinders are simulated by using Fluent software. The simulation results show that the new type of Flettner rotor system has a remarkable effect.

The main results that can be drawn are as follows:

1. This study compares the lift and thrust coefficients of two rotating cylinders when the two rotating cylinders are installed side by side. The lift coefficients of the rotating cylinders increase with the increase in spin ratio. The maximum lift coefficient occurs when the spin ratio is 3.0. In addition, the apparent wind angle also affects the performance of the rotating cylinders. The lift coefficients of the two rotating cylinders are at a minimum when the apparent wind angle is 90°; the lift coefficients of the two rotating cylinders are at a maximum at an apparent wind angle of 150°. Therefore, the maximum lift coefficients of cylinder *A* and cylinder *B* are 11.98 and 10.68, respectively, at an apparent wind angle θ=150° and spin ratio α=3.0. Because thrust coefficient depends on the lift coefficient, the drag coefficient and the apparent wind angle, the maximum lift coefficient of the rotating cylinder does not mean that the thrust contribution of the rotating cylinders reaches its peak value. The maximum thrust coefficient of cylinder *A* (corresponding to a spin ratio of 3.0) occurs when the apparent wind angle is 90°, which is 10.54; when the apparent wind angle is 120° and the spin ratio is 3.0, the maximum thrust coefficient of cylinder *B* is 10.38.

2. The pressure distributions of two rotating cylinders with different spin ratios and an apparent wind angle of 90° are compared. It can be seen that the pressure differences around the two rotating cylinders along the y-axis become larger with an increase in spin ratio. Under the conditions of the same spin ratio, it can be seen that, when the apparent wind angle is 120°, the total thrust of the two rotating cylinders reaches a peak value, which can reach 500 kN.

3. The thrust contribution of the two rotating cylinders increases with the increase in spin ratio. The maximum thrust power is 2575 kW at the apparent wind angle of 120° under a spin ratio of 3.0. Moreover, when the spin ratio increases, the effective power first increases and then decreases. When the apparent wind angle is 60°-120°and the spin ratio is 2.5, the maximum effective power is obtained. The maximum effective power in the other two apparent wind angles corresponds to the spin ratio of 2.0.

4. When the two rotating cylinders are in different positions, it is found that the lift coefficients of the two rotating cylinders increase with an increase of spin ratio. The maximum lift coefficient of cylinder *A* is obtained when the distance between the two rotating cylinders is 7D and the spin ratio is 3.0; the lift coefficient of the cylinder *B* is obtained when the distance between the two rotating cylinders is 13D and the spin ratio is 3.0. In addition, when the distance between the two rotating cylinders is 10D and the spin ratio is 3.0, the total thrust of the two cylinders is 530 kN, and the maximum thrust power is 2677 kW. By comparing the effective power of the two rotating cylinders at different positions, it is found that the maximum effective power is 1932 kW when the distance between the two rotating cylinders is 7D.

This study provides a useful reference for practical engineering applications.

ACKNOWLEDGEMENTS

This project was funded by the Natural Science Foundation of Shandong Province of China (ZR2021ME156).

REFERENCES

1. L. Zhu, B.L. Li, A. Li, W.X. Ji, Y. Qian, X.C. Lu and Z. Huang. 'Effects of fuel reforming on large-bore low-speed two-stroke dual fuel marine engine combined with EGR and injection strategy'. International Journal of Hydrogen Energy, 45, 2020. 29505-29517. doi: 10.1016/j.oceaneng.2019.01.026.
2. ICCT, The international maritime organization's initial greenhouse gas strategy. Update Policy, 2018. 3–4.
3. A. Halff, L. Younes and T. Boersma, 'The likely implications of the new IMO standards on the shipping industry'. Energy Policy, 126, 2019. 277–286. doi: 10.1016/j.enpol.2018.11.033.
4. S.L. Wen, H. Lan, Y.Y. Hong, D.C. Yu, L.J. Zhang and P. Cheng. 'Allocation of ESS by interval optimization method considering impact of ship swinging on hybrid PV/diesel ship power system'. Applied Energy, 175, 2016. 158–167. doi: 10.1016/j.apenergy.2016.05.003.
5. F. Diab, H. Lan and S. Ali, 'Novel comparison study between the hybrid renewable energy systems on land and on ship'. Renewable and Sustainable Energy Reviews, 63, 2016. 452–463. doi: 10.1016/j.rser.2016.05.053.
6. P.C. Pan, Y.W. Sun, C.Q. Yuan, X.P. Yan and X.J. Tang. 'Research progress on ship power systems integrated with new energy sources: A review'. Renewable and Sustainable Energy Reviews, 144, 2021. 111048. doi: 10.1016/j.rser.2021.111048.
7. J.H. He, Y.H. Hu, J.J. Tang and S.Y. Xue. 'Research on sail aerodynamics performance and sail-assisted ship stability'. Journal of Wind Engineering and Industrial Aerodynamics, 146, 2015. 81-89. doi: 10.1016/j.jweia.2015.08.005.
8. L. Talluri, D.K. Nalianda and E. Giuliani, 'Techno economic and environmental assessment of Flettner rotors for marine propulsion'. Ocean Engineering, 154, 2018. 1–15. doi: 10.1016/j.oceaneng.2018.02.020.
9. N.J. Van Der Kolk, I. Akkerman, J.A. Keuning and R.H.M. Huijsmans. 'Part 2: Simulation methodology and numerical uncertainty for RANS-CFD for the hydrodynamics of wind-assisted ships operating at leeway angles'. Ocean Engineering, 201, 2020. 107024. doi: 10.1016/j.oceaneng.2020.107024.
10. Y. Ma, H.X. Bi, M.Q. Hu, Y.Z. Zheng and L.X. Gan. 'Hard sail optimization and energy efficiency enhancement for sail-assisted vessel'. Ocean Engineering, 173, 2019. 687–699. doi: 10.1016/j.oceaneng.2019.01.026.
11. R.H. Lu and J.W. Ringsberg. 'Ship energy performance study of three wind-assisted ship propulsion technologies including a parametric study of the Flettner rotor technology'. Ships and Offshore Structures, 15, 2020. 249-258. doi: https://doi.org/10.1080/17445302.2019.1612544. doi: 10.1080/17445302.2019.1612544.
12. F. Tillig and J.W. Ringsberg. 'Design, operation and analysis of wind-assisted cargo ships'. Ocean Engineering, 211, 2020. Article ID 107603. doi: 10.1016/j.oceaneng.2020.107603.
13. I.S. Seddiek and N.R. Ammar. 'Harnessing wind energy on merchant ships: case study Flettner rotors onboard bulk carriers'. Environmental Science and Pollution Research, 28, 2021. 32695–32707. doi: 10.1007/s11356-021-12791-3.

14. S. Pezzotti, V.N. Mora, A.S. Andres and S. Franchini. 'Experimental study of the Magnus effect in cylindrical bodies with 4, 6, 8 and 10 sides'. Journal of Wind Engineering & Industrial Aerodynamics, 197, 2020. 104065. doi: 10.1016/j.jweia.2019.104065.

15. L.C. Correa, J.M. Lenz, C.G. Ribeiro and F.A. Farret. 'Magnus Wind Turbine Emulator With MPPT by Cylinder Rotation Control'. Journal of Dynamic Systems, Measurement, and Control, 140, 2018. 101012. doi: 10.1115/1.4040212.

16. A. De Marco, S. Mancini, C. Pensa, G. Calise and F. De Luca. 'Flettner rotor concept for marine applications: a systematic study'. International Journal of Rotating Machinery. 2016. 12. Article ID 3458750. doi: 10.1155/2016/3458750.

17. B.Y. Li, R. Zhang, B.S. Zhang, Q.Q. Yang and C. Guo. 'An assisted propulsion device of vessel utilising wind energy based on Magnus effect'. Applied Ocean Research, 114 (2021), Article ID 102788. doi: 10.1016/j.apor.2021.102788.

18. G. Bordogna, S. Muggiasca, S. Giappino, M. Belloli, J.A. Keuning, R.H.M. Huijsmans and A.P. van 't Veer. 'Experiments on a Flettner rotor at critical and supercritical Reynolds numbers'. Journal of Wind Engineering and Industrial Aerodynamics, 188 (2019), 19–29. doi: 10.1016/j.jweia.2019.02.006.

19. G. Bordogna, S. Muggiasca, S. Giappino, M. Belloli, J.A. Keuning and R.H.M. Huijsmans. 'The effects of the aerodynamic interaction on the performance of two Flettner rotors'. Journal of Wind Engineering and Industrial Aerodynamics, 196, 2020. 104024. doi: 10.1016/j.jweia.2019.104024.

20. B.Y. Li, R. Zhang, Y.J. Li, B.S. Zhang and C. Guo. 'Study of a new type of Flettner rotor in merchant ships'. Polish Maritime Research, 109 (2021), 28-41. doi: 10.2478/pomr-2021-0003.

21. J. Seifert. 'A review of the Magnus effect in aeronautics'. Progress in Aerospace Sciences, 55, 2012. 17-45. doi: 10.1016/j.paerosci.2012.07.001.

22. X.Y. Liu, Y.X. Wang, J.J. Liang and S. Wang. 'CFD Analysis of Aerodynamic Characteristics of Ship's Wind-Assisted Rotor Sail. Navigation of China', doi: 1000-4653, 2019. 04-0046-05.

23. X.Y. Lu. 'Study on aerodynamic Performance of Vertical Magnus Wind Turbine'. University of Xiang Tan, May 2019.

24. A. Sedaghat, I. Samani, M. Ahmadi-Baloutaki, M.E.H. Assad and M. Gaith. 'Computational study on novel circulating aerofoils for use in Magnus wind turbine blades'. Energy, 91, 2015. 393-403. doi: 10.1016/j.energy.2015.08.058.

25. N.R. Ammar and I.S. Seddiek. 'Enhancing energy efficiency for new generations of containerized shipping'. Ocean Engineering, 215, 2020. 107887. doi: 10.1016/j.oceaneng.2020.107887.

26. M. Traut, P. Gilbert, C. Walsh, A. Bows, A. Filippone, P. Stansby and R. Wood. 'Propulsive power contribution of a kite and a Flettner rotor on selected shipping routes'. Applied Energy, 113, 2014. 362–372.

27. D. Moreira, N. Mathias, T. Morais. 'Dual flapping foil system for propulsion and harnessing wave energy: A 2D parametric study for unaligned foil configurations'. Ocean Engineering, 215 (2020), 107875. doi: 10.1016/j.oceaneng.2020.107875.

28. D. Wang and PL-F. Liu. 'An ISPH with k–ε closure for simulating turbulence under solitary waves'. Coastal Engineering, 157, 2020. 103657. doi: 10.1016/j.coastaleng.2020.103657.

29. B.S. Zhang, B.W. Song, Z.Y. Mao, W.L. Tian, B.Y. Li and B. Li. 'A novel parametric modeling method and optimal design for savonius wind turbines'. Energies. 10 (2017), 301. doi: 10.3390/en10030301.

30. D.J. Wang, K. Liu, P. Huo, S.Q. Qiu, J.W. Ye and F.L. Liang. 'Motions of an unmanned catamaran ship with fixed tandem hydrofoils in regular head waves'. Journal of Marine Science and Technology. 24, 2019. 705-719. doi: 10.1007/s00773-018-0583-x.

31. C. Badalamenti and S.A. Prince. 'Effects of endplates on a rotating cylinder in crossflow'. In Proceedings of the 26th AIAA Applied Aerodynamics Conference, Honolulu, Hawaii, USA, August 2008.

32. A. De Marco, S. Mancini, C. Pensa, 'Preliminary analysis for marine application of Flettner rotors' in Proceedings of the 2nd International Symposium on Naval Architecture and Maritime (INT-NAM '14), Istanbul, Turkey, October 2014.

33. A. De Marco, S. Mancini, C. Pensa, R. Scognamiglio and L. Vittiello. 'Marine application of Flettner rotors: numerical study on a systematic variation of geometric factor by doe approach'. In Proceedings of the 6th International Conference on Computational Methods in Marine Engineering (MARINE'15), Rome, Italy, June 2015.

34. I.S. Seddiek and N.R. Ammar. 'Harnessing wind energy on merchant ships: case study Flettner rotors onboard bulk carriers'. Environmental Science and Pollution Research, 28, 2021. 32695–32707. doi: 10.1007/s11356-021-12791-3.

CONTACT WITH THE AUTHORS

Jingze Lv
College of Electromechanical Engineering,
Qingdao University of Science and Technology,
Qingdao 266061, Shandong, China,
China

Yiqun Lin
College of Electromechanical Engineering,
Qingdao University of Science and Technology,
Qingdao 266061, Shandong, China,
China

Rui Zhang
College of Electromechanical Engineering,
Qingdao University of Science and Technology,
Qingdao 266061, Shandong, China,
China

Boyang Li
e-mail: qdlby@126.com

College of Electromechanical Engineering,
Qingdao University of Science and Technology,
Qingdao 266061, Shandong, China,
China

Hualin Yang
College of Electromechanical Engineering,
Qingdao University of Science and Technology,
Qingdao 266061, Shandong, China,
China